MATERIALS CHEMISTRY
FRONTIERS

CHINESE CHEMICAL SOCIETY

ROYAL SOCIETY OF CHEMISTRY

RESEARCH ARTICLE

View Article Online
View Journal

Cite this: DOI: 10.1039/d5qm00794a

Molecular and supramolecular room temperature phosphorescences from metal free carbonyl functionalized triazinic scaffold

Daniele Malpicci,[ab] Daniele Marinotto,[b] Elena Lucenti,[b] Luca Zecchinello,[ab] Chiara Botta,[c] Alessandra Forni*[b] and Elena Cariati*[ab]

Received 8th November 2025,
Accepted 26th January 2026

DOI: 10.1039/d5qm00794a

rsc.li/frontiers-materials

The photophysical behavior in solution, PMMA films and crystals of PhCHO mono-, **TTPhCHO**, and tri-substituted, **TT(PhCHO)$_3$**, cyclic triimidazole (**TT**) derivatives is here reported and analyzed through computational and X-ray diffraction studies. The two compounds are poorly fluorescent in diluted solution but display aggregation-induced emissive, AIE, behavior in the solid state where molecular and multiple supramolecular long lived radiative deactivation channels are turned on. In particular, in PMMA films, **TTPhCHO** is mailny fluorescent while **TT(PhCHO)$_3$** is only phosphorescent. In crystals, both compounds show exclusively long lived components of molecular (HEP), CHO···TT (MEP) and π–π (TT-TT or TT-Ph, LEP) supramolecular origin as disclosed through theoretical and single crystal X-ray diffraction analysis. The different behaviour observed in PMMA films has been assigned to the easier S–T intersystem crossing associated with the three *vs.* one carbonyl substituents in **TT(PhCHO)$_3$** and **TTPhCHO**, respectively.

Introduction

Purely organic materials showing room temperature phosphorescence (RTP) are garnering increasing attention from the scientific community due to their applicability in several fields spanning from light-emitting diodes[1–3] to anticounterfeiting and data encryption,[4–10] time-gated bioimaging,[11–16] and 3D displays,[17–20] offering clear advantages with respect to the inorganic counterparts, like broad spectral tunability, low toxicity, and biocompatibility.[21,22]

Typical strategies to obtain organic RTP materials include, on one side, incorporation of heavy halogen atoms or functional groups containing N, O or P atoms with lone-pair electrons, able to increase the intrinsically weak Spin–Orbit coupling (SOC) through accessible (n,π*) transitions. Particularly relevant in this regard are aromatic carbonyl-based materials, exhibiting highly efficient ultralong organic phosphorescence in the solid state due to the coupling of (n,π*) and (π,π*) excited-states.[23] On the other side, structural rigidification at room temperature can reduce the molecular motions responsible for nonradiative decay and protect the triplet excitons from oxygen. To this aim, several approaches, such as crystallization-induced phosphorescence,[24,25] host–guest system,[26–30] H-aggregation,[31,32] polymerization[33] or doped polymers[34–37] have been proposed resulting in the stabilization of the triplet state. Among these strategies, the incorporation of phosphorescent dopants in polymeric matrices has been pursued for the development of multifunctional RTP materials endowed with appealing processability. In this context, multicolor and mechano-responsive 3D printable materials with tunable properties have been prepared by integrating imidazole-based chromophores into different polymeric matrices.[38] The rigid molecular environment provides RTP films suitable for applications in anticounterfeiting, afterglow display and as visual frequency indicators.[39] Stretchable afterglow hydrogels for digital light processing 3D printing technology and anti-counterfeiting encryption have been realized by introducing afterglow microcrystals within various hydrogels.[40]

On the other side, crystal engineering through intermolecular interactions of the organic building block has been widely employed as a strategy for the design and realization of molecular architectures with RTP properties.[41]

Frequently, intermolecular interactions are able not only to stabilize emitting states but also to generate supramolecular structures characterized by their own radiative deactivation channels.[42–45] Among others, it has been demonstrated[46] that aromatic aldehydes and ketones can promote RTP through intermolecular electronic coupling (IEC) of the carbonyl and

---

[a] *Department of Chemistry, Università degli Studi di Milano, via Golgi 19, 20133 Milano, Italy. E-mail: elena.cariati@unimi.it*
[b] *Institute of Chemical Sciences and Technologies "Giulio Natta" (SCITEC) of CNR, via Golgi 19, 20133 Milano, Italy. E-mail: alessandra.forni@scitec.cnr.it*
[c] *Institute of Chemical Sciences and Technologies "Giulio Natta" (SCITEC) of CNR, via Corti 12, 20133 Milano, Italy*

aromatic subunits thanks to their different (*i.e.* (n,π*) and (π,π*)) excited-state configurations. Such mechanism requires proximity and a specific geometrical arrangement of the two moieties within the crystal structure, with the carbonyl group of one molecule stacked approximately parallel to the aromatic group of a neighboring molecule.

Understanding the relationship between intermolecular interactions and RTP features of organic materials is therefore crucial to improve the material design process and optimize their performance in devices.

In this context, in the last decade we have explored an extended series of organic compounds based on triimidazo[1,2-*a*:1′,2′-*c*:1″,2″-*e*][1,3,5]triazine or cyclic triimidazole (from hereafter **TT**), characterized by a rich photophysical behavior comprising multiple fluorescence and phosphorescence of molecular and supramolecular origins, anti-Kasha emissions and excitation dependent photoluminescence.[47] **TT** prototype itself displays aggregation-induced emissive, AIE, features including ultralong phosphorescence (up to 1 s) under ambient conditions associated with the presence of strong π–π stacking interactions in its crystalline structure.[32] It has been demonstrated how the introduction of halogens, ethynyl, carboxyl and various chromophoric (such as pyrene, pyridines, carbazole and thiophene) groups on the **TT** scaffold allows not only to preserve, in most cases, RTP of π–π stacked origin, but also to activate molecular RTP and, in some cases, additional supramolecular short- or long-lived contributions associated with either hydrogen bonding, HB,[43,48] or extrinsic and intrinsic heavy atom effects.[49]

Here, an investigation on the role of the carbonyl group on the photophysical behavior of **TT** functionalized with one or three benzaldehyde groups, namely 4-(triimidazo[1,2-*a*:1′,2′-*c*:1″,2″-*e*][1,3,5]triazin-3-yl)benzaldehyde, **TTPhCHO**, and 4,4′,4″-(triimidazo[1,2-*a*:1′,2′-*c*:1″,2″-*e*][1,3,5]triazine-3,7,11-triyl)tribenzaldehyde, **TT(PhCHO)$_3$**, is reported. It is shown that these derivatives are characterized by intriguing AIE behavior. The two compounds show, in fact, weak fluorescence in solution but multiple molecularly and supramolecularly induced phosphorescences in the aggregated phases. In particular, π–π stacked aggregates and the related RTP contribution, together with IEC-based RTP, associated with the presence of short carbonyl···TT contacts, are observed for both compounds.

Results and discussion

TTPhCHO and **TT(PhCHO)$_3$** were prepared by Suzuki coupling between 4-formylphenylboronic acid MIDA ester and the corresponding mono- (**TTBr**) or tri-brominated (**TTBr$_3$**) **TT**-derivative, respectively (see Experimental and Scheme 1). Both compounds have been characterized by single crystal X-ray diffraction and multinuclear ^{1}H, ^{13}C NMR spectroscopy in solution (see Fig. S1–S10). Importantly, since multiple emissions are often to be associated with impurities, many batches of the compounds were photophysically analyzed to assess reproducible behaviors and exclude contaminations.

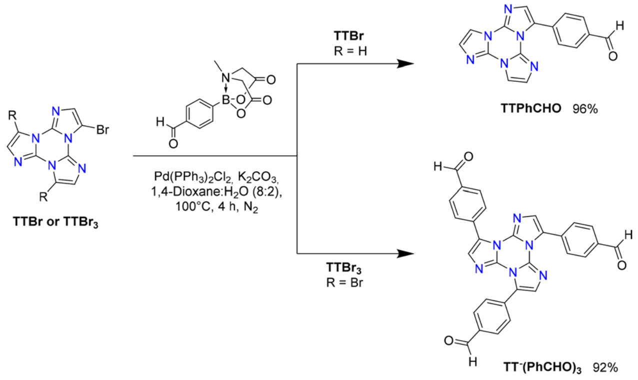

Scheme 1 Synthesis of **TTPhCHO** and **TT(PhCHO)$_3$**.

The two compounds display superimposable absorption and emission spectra in diluted DCM solution (1 × 10^{-5} M, see Fig. 1 and Table 1) characterized by an absorption at about 320 nm and a broad, weak fluorescence centered at 374 nm (*Φ* = 0.8 and 0.6%, *τ* = 1.6 and 2.0 ns, Fig. S13 and S21, for **TTPhCHO** and **TT(PhCHO)$_3$**, respectively).

To assess the molecular optical behavior in a rigid environment at RT, diluted (0.5 w/w%) spin-coated films were prepared using PMMA as matrix due to its effectiveness in restricting molecular motions and reducing non-radiative deactivation channels.[38,47,50] Films of the two compounds display similar absorption features (λ_{max} = 320 nm) but quite different steady-state excitation dependent photoluminescent behavior (Fig. 2). The similarity of absorption maxima in PMMA matrix and DCM solutions indicates that chromophores in films exist predominantly in a monodispersed state. However, minor contributions from aggregated species must be considered also at low loading, especially in the emissive patterns (here confirmed by the different DCM absorption and PMMA excitation spectra of both compounds, see Fig. S11 and S12). In fact, aggregation induced emissions (AIE) are observed for both compounds. At 300 nm excitation, the photoluminescence, PL, spectrum of both compounds in PMMA is characterized by a multicomponent emission. More in detail, PL of **TTPhCHO** is

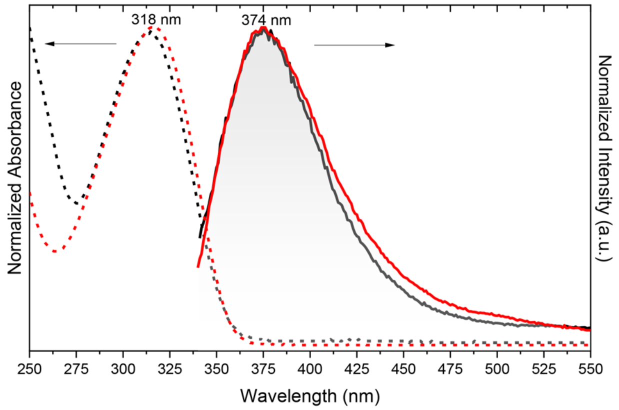

Fig. 1 Normalized absorption (dashed lines) and emission (full lines, λ_{exc} = 300 nm) of DCM (1 × 10^{-5} M) solution of **TTPhCHO** (black) and **TT(PhCHO)$_3$** (red).

Table 1 Photophysical parameters of **TTPhCHO** and **TT(PhCHO)$_3$**

		298 K			77 K	
		Φ (%)	λ_{em} (nm)	τ_{av}	λ_{em} (nm)	τ_{av} (ms)
TTPhCHO	DCM	0.8	374	1.64 ns		
	PMMA	0.7	360	1.35 ns		
			434	488 µs		
			470			
			530	3.38 ms		
	Crystals	7	430	123.6 µs		1.00
			480		473	
			560	6.01 ms	534	47.86
TT(PhCHO)$_3$	DCM	0.6	374	2.02 ns		
	PMMA	1.3	434	147.3 µs		
			555	90.6 µs		
	Crystals	0.8	410	536.2 µs	420	1.84
			>430	3.92 ms	465	11.8
			575	10.5 ms	570	65.7

dominated by a narrow fluorescence centered at 360 nm (Φ = 0.7%, τ = 1.3 ns, Fig. S14), resembling the emission in DCM solution, together with additional low energy tails at about 435 and 500 nm (Fig. 2 upper panel, left). On the other hand, **TT(PhCHO)$_3$** shows a PL spectrum quite different from that collected in DCM comprising only one broad band with recognizable maxima at about 430 and 500 nm (Φ = 1.3%, Fig. 2 bottom panel, left). The different contributions can be better isolated by varying excitation wavelength. For **TTPhCHO**, the low energy components (at 430 and 500 nm) can be activated at the expense of the otherwise prevailing higher energy fluorescence by exciting at 360 and 430 nm (Fig. 2, upper panel, right), respectively. At the same excitation wavelengths, **TT(PhCHO)$_3$** shows better resolved spectra with emissions at 430 and 525 nm, respectively (Fig. 2, bottom panel, right). From lifetime measurements, all emissions except for the 360 nm one of **TTPhCHO**, can be classified as phoshporescences (see Table 1 and Fig. S15, S16, S27 and S28).

To better investigate the long-lived components, we collected for both compounds delayed emission spectra of their PMMA films. Intriguingly, for **TTPhCHO** three different long-lived emissions are recognized when emission is collected at different delay times and integrated in different time windows (see Fig. 3,

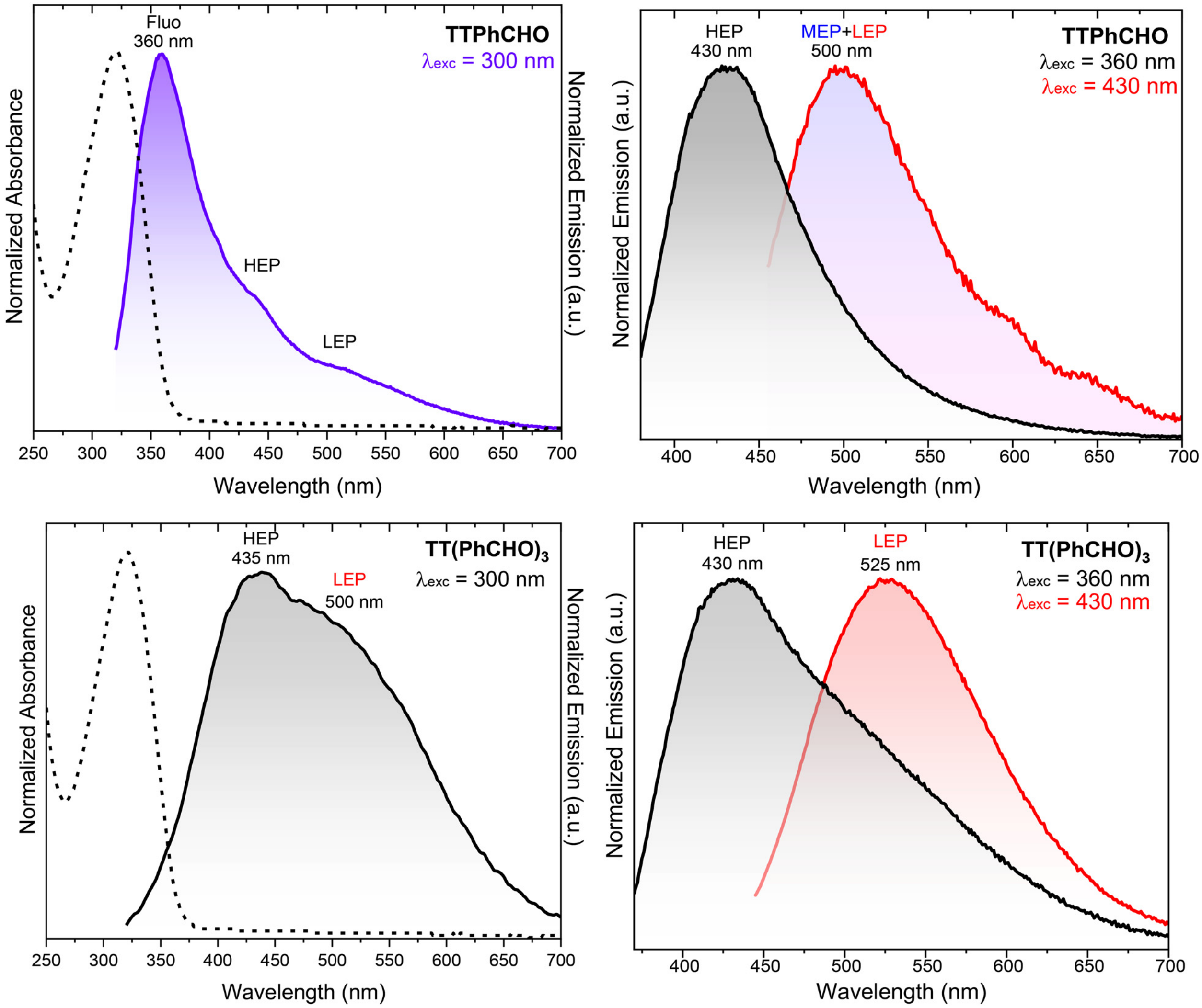

Fig. 2 Normalized Spectra of PMMA film (0.5 w/w%) of **TTPhCHO** (upper panel) and **TT(PhCHO)$_3$** (bottom panel) at 298 K. Left: absorption (dash lines) and PL emission (full lines, λ_{exc} = 300 nm). Right: PL emission at λ_{exc} = 360 (black lines) and 430 nm (red lines).

left): (i) at short delay (50 μs) a high energy phosphorescence (HEP) superimposable to the 434 nm emission observed in steady-state experiments; (ii) at longer delay (200 μs) a medium energy phosphorescence (MEP) centered at 470 nm, which was not revealed through steady-state spectra; (iii) by extending the time window up to 5 ms a low energy phosphorescence (LEP) is recognized at 530 nm. This latter corresponds to the 500 nm one observed in steady-state spectrum with maximum position affected by the presence of the higher energy contributions. In the case of **TT(PhCHO)$_3$**, analogously to steady-state measurements, two broad phosphorescences are evidenced in the delayed spectra (Fig. 3, right): a vibronically resolved HEP with maximum at 434 nm, closely matching the 430 nm PL emission, and LEP centered at 555 nm. This latter again shifted to lower energy with respect to its PL analogue where the presence of the higher energy component affects the emission wavelength. Despite measurements in various experimental conditions (excitation wavelength, time delays and time windows) the presence of a medium energy phosphorescence, similar to **TTPhCHO**, was not evidenced. However, this contribution could be hidden by the broad HEP probably having similar lifetimes.

The photoluminescent behaviour of the two compounds was further investigated on crystalline samples (see Fig. 4 and 5). A notable result in this respect is the absence of fluorescent

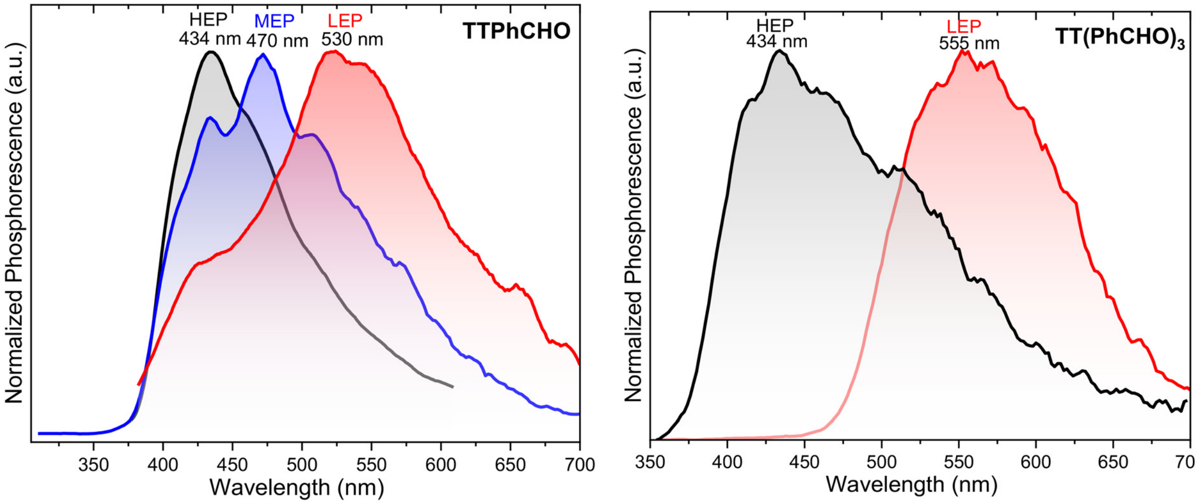

Fig. 3 Normalized Phosphorescence spectra at 298 K of PMMA film (0.5 w/w%) of **TTPhCHO** (left: black line, λ_{exc} = 250 nm, delay 50 μs, window 0.5 ms; blue line, λ_{exc} = 280 nm, delay 0.2 ms, window 0.5 ms; red line, λ_{exc} = 300 nm, delay 0.1 ms, window 5 ms) and **TT(PhCHO)$_3$** (right: red line, λ_{exc} = 330 nm, delay 0.2 ms, window 0.5 ms; black line, λ_{exc} = 250 nm, delay 1 ms, window 5 ms).

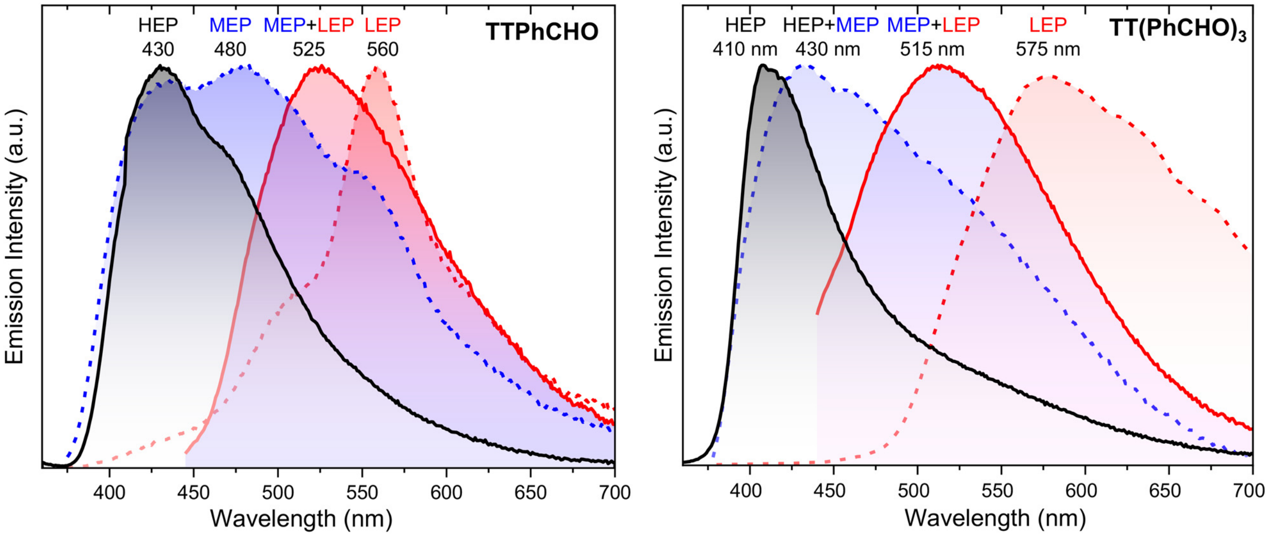

Fig. 4 Normalized PL and Phosphorescence spectra of crystals of **TTPhCHO** (left) and **TT(PhCHO)$_3$** (right) at 298 K. Left: prompt (full lines: black, λ_{exc} = 340 nm; red, λ_{exc} = 430 nm) and delayed emissions (dashed λ_{exc} = 300 nm: blue, delay 20 μs, window 0.1 ms; red, delay 50 μs, window 0.5 ms). Right: prompt (full lines: black, λ_{exc} = 340 nm; red, λ_{exc} = 420 nm) and delayed emissions (λ_{exc} = 340 nm, blue, delay 20 μs, window 200 μs; red, delay 100 μs, window 1 ms).

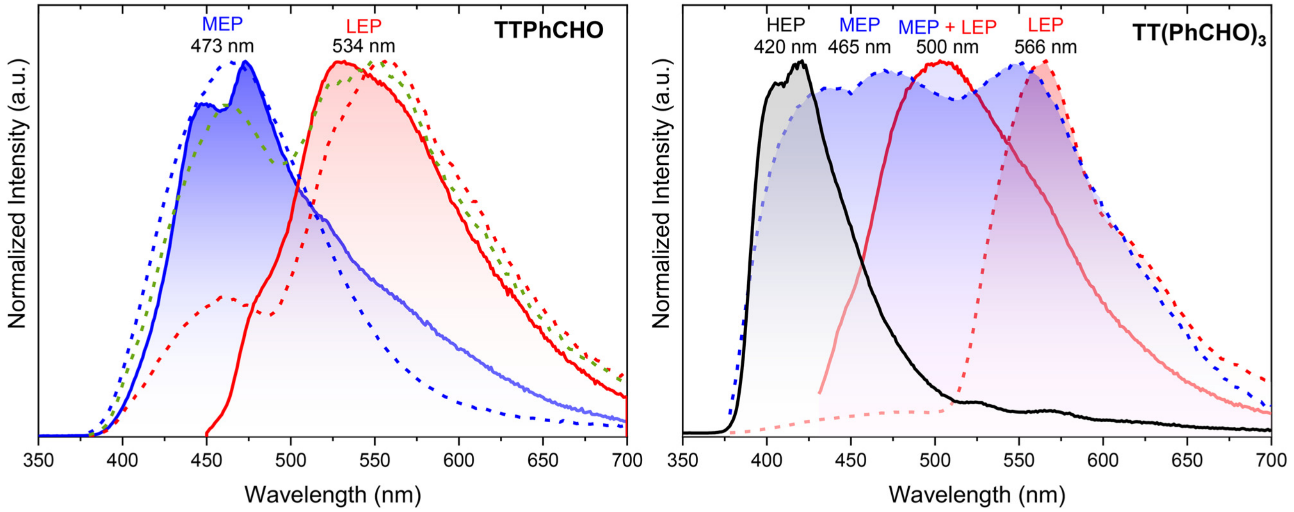

Fig. 5 Normalized PL (77 K) and phosphorescence (87 K) spectra of crystals of **TTPhCHO** (left) and **TT(PhCHO)$_3$** (right). Left: prompt (full lines: blue, λ_{exc} = 300 nm; red, λ_{exc} = 430 nm) and delayed emissions (dashed lines, λ_{exc} = 300 nm: blue, delay 20 μs window 100 μs; green, delay 500 μs window 2 ms, red, delay 2 ms window 2 ms). Right: prompt (full lines black, λ_{exc} = 300 nm; red, λ_{exc} = 420 nm) and delayed emissions (dashed lines, λ_{exc} = 340 nm: blue, delay 20 μs, window 200 μs; red, delay 200 μs, window 2 ms).

emission for both crystalline systems regardless of excitation wavelength. More in details, in the 298 K PL spectrum of **TTPhCHO** crystals, HEP (at 430 nm, τ = 123.6 μs, Fig. S17) and LEP (at 525 nm, τ = 6.01 ms, Fig. S18) are observed, both having clear contribution from MEP, by exciting at 340 and 430 nm, respectively (Fig. 4 left, solid lines). HEP, MEP and LEP (at 430, 480 and 560 nm, respectively) are better resolved in delayed emission spectra by varying the time delay and integration time window (Fig. 4 left, dashed lines). On the contrary, for **TT(PhCHO)$_3$** the presence or absence of MEP cannot, again, be unambiguously established by room-temperature measurements. More specifically, HEP at about 410 nm (τ = 536.2 μs, Fig. S29) is clearly recognized in both steady state and delayed spectra (Fig. 4 right) together with an additional lower energy phosphorescence. This latter is centered at 515 nm (τ = 3.92 ms, Fig. S30) in the steady state spectrum and at 575 nm in the delayed one suggesting the presence of different contributions in the broad 515 nm PL emission. For this reason, we have monitored lifetimes at 575 nm obtaining a significantly longer τ (τ = 10.5 ms, Fig. S31) unambiguously indicating concomitant MEP and LEP in the 515 nm broad emission.

To better disclose different contributions in the emission spectra, we have performed variable temperature spectral analysis. Intriguingly, at 77 K and 300 nm excitation MEP of **TTPhCHO** crystals, hardly visible in the 298 K PL spectra, becomes dominant (at 473 nm, τ = 1.00 ms, Figure S19) over HEP and LEP, this latter resolved (at 534 nm, τ = 47.86 ms, Figure S20) at 430 nm excitation (Fig. 5 left). The different lifetimes of MEP and LEP are evidenced in the LT delayed spectra by varying time delays and integration windows. In fact, at 77 K for short integration times (<150 μs) MEP is by far the dominant emission; LEP is recognized when integration windows are extended to 1–2 ms, being the main contribution at delays larger than 500 μs (Fig. S22). The temperature dependence of delayed spectra is also indicative of the different origin of the phosphorescences. At short times, MEP dominates the spectrum at any temperature below RT (see Fig. S22–S24). At intermediate times, LEP appears at 140 K by cooling from RT (Fig. S23). For longer times (integration windows of 2 ms), LEP is the main phosphorescence at any temperature (Fig. S22–S26).

For **TT(PhCHO)$_3$**, HEP (at 420 nm, τ = 1.84 ms, Fig. S32) and LEP (at 500 nm, τ = 11.8 ms, Fig. S33) are evidenced at 77 K by exciting at 300 and 420 nm, respectively (Fig. 5 right).

In time delayed experiments at low temperature, all three phosphorescences are concomitantly observed at short times (delay 20 μs, window 200 μs), while LEP is by far the dominant emission for delays larger than 200 μs (Fig. 5 and Fig. S36). The delayed spectra recorded at short times by lowering the temperature allow to recognize a spectral evolution from HEP (RT) to HEP + MEP (250 K) to HEP + MEP + LEP (150 K), see Fig. S37.

To better interpret the photophysical behavior of the two compounds, we performed a systematic theoretical study and a comparative analysis of their crystal structures, aimed at elucidating molecular and supramolecular features involved in the emissive processes.

The DFT optimized 'gas-phase' **TTPhCHO** and **TT(PhCHO)$_3$** molecular structures are weakly or scarcely polar (μ = 3.14 and 1.46 D, respectively). Their TDDFT excitation spectra are almost overlapped (Fig. S40–S41 and Tables S2–S3) and consist of one low energy strong band, which corresponds to states S_2 and S_2' for **TTPhCHO** and **TT(PhCHO)$_3$**, respectively. The prime refers to the fact that, in the triply substituted derivative, levels have threefold degeneration, so S_1' refers to $\{S_1, S_2, S_3\}$, S_2' to $\{S_4, S_5, S_6\}$, and so on. S_1 and S_1' have (σ, π*) character, with almost vanishing oscillator strength and therefore not observed in the UV-vis spectra. They mainly involve inner HOMO(s) and the LUMO(s), both of them localized on the PhCHO group(s). S_2 and S_2', instead, correspond to strong (π,π*) transitions mainly involving HOMO(s), delocalized on the whole molecule, and LUMO(s) localized on the PhCHO group(s). For both compounds, calculations on the ground state geometry provide a triplet state (T_3 and T_3') with (π,π^*) character, located below S_1 and S_1' by ΔE_{S-T} = 0.14 and 0.02 eV for **TTPhCHO** and **TT(PhCHO)$_3$**, respectively, suggesting easy singlet-to-triplet intersystem crossing (ISC) based on both the different character of the two states (El-Sayed rule) and their small energy difference. Optimization of S_1 converges in both cases to a geometry very similar to the ground state one, maintaining the same (σ, π^*) character of the Franck–Condon state. Including SOC in TDDFT calculations provides triplet states T_2 which are located below S_1 by 0.37 and 0.34 eV for **TTPhCHO** and **TT(PhCHO)$_3$**, respectively (Fig. 6). Though similar S_1–T_2 SOC elements are obtained for the two compounds (24 and 17 cm^{-1}, respectively), it should be considered that, in **TT(PhCHO)$_3$** three degenerate relaxed S_1 states (rather than the single one in **TTPhCHO**) contribute to determine the singlet-to-triplet ISC, therefore indicating an easier population of triplet exciton with respect to the mono-substituted compound.

Based on these results, it is expected that excitation at 300 nm populates both S_1 and S_2, and the weak fluorescence observed in solution, with relatively small (0.66 eV) Stokes shift, is imputable to emission from S_1 (eventually after internal conversion, IC, from S_2), having very low oscillator strength. In PMMA and crystals, the highly favorable S_1–T_2 ISC becomes competitive with respect to radiative decay from S_1, thanks to rigidification effects (through the matrix or intermolecular interactions) which inhibit non-radiative decay paths, explaining observation of HEP for both compounds. This long-lived contribution can, in fact, be originated by radiative decay from T_1 (computed at 418 nm for both compounds) after IC from T_2. This attribution agrees with its predominance and coincident position (435 nm) in PMMA films of both compounds. Moreover, S_1–T_2 ISC is expected to be particularly efficient in **TT(PhCHO)$_3$** owing to the presence of three carbonyl groups with associated three-fold degeneration of S_1, thus explaining the lack of fluorescence in its solid phases (PMMA and crystals).

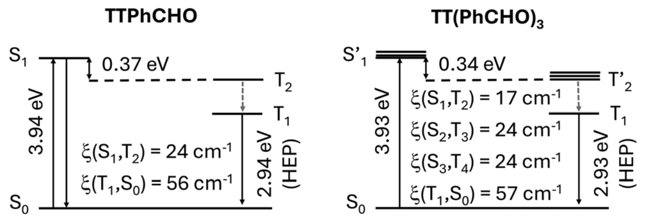

Fig. 6 Computed energy diagram and spin orbit coupling matrix elements (ξ) for **TTPhCHO** (left) and **TT(PhCHO)$_3$** (right).

To interpret the additional long-lived, lower-energy contributions, supramolecular emissive species should be invoked and to do so we have deeply analyzed the single crystal structure of both compounds.

TTPhCHO crystallizes in the *P*2/*n* space group with two molecules per asymmetric unit (Table S1, Fig. 7 and Fig. S38). The two independent molecules, labelled with A and B, display the same distortion of the phenyl ring with respect to the TT unit (the dihedral angle between the two units measuring 50.9°), but opposite orientation of the CHO group, which is otherwise coplanar to the phenyl. DFT geometry optimization of A and B provides the same stability for the two conformations. In the crystal structure, the two molecules form, along the crystallographic direction *b*, segregate columnar aggregates …AAA… and …BBB… with identical interlayer separation, held together through π–π stacking interactions and further stabilized by sheared parallel CO···CO ones (Fig. 7, left).[51] The distance between triazinic geometrical centroids measures 3.877 Å, denoting quite reduced slippage along the stack. A and B are related to one another by a pseudo-inversion center and are connected, on the TT side, through short C–H···N hydrogen bonds, HBs, ($r_{\text{H5A}\cdots\text{N5B}}$ = 2.38 Å and $r_{\text{H5B}\cdots\text{N5A}}$ = 2.51 Å), with TT units lying on almost parallel planes separated by about 0.6 Å. On the PhCHO side, both molecules are in turn linked to their respective centrosymmetry-related partner through CO···CO interactions according to a slightly sheared antiparallel motif ($r_{\text{C16A}\cdots\text{O1A}'}$ = 3.190(3) Å and $r_{\text{C16B}\cdots\text{O1A}''}$ = 3.383(3) Å).[51] As a result, infinite non-parallel ···A···A···B···B···A···A··· chains are formed, laterally interacting with each other through C–H···N, C–H···O and C–H···π HBs (Fig. 7, right). Moreover, a short contact between the carbonyl group of A and the TT moiety of B is present ($r_{\text{O1A}\cdots\text{C1B}}$ = 3.129(3) Å), with the two subunits lying on almost parallel planes (the dihedral angle through their least-squares planes is equal to 4.95°, see Fig. 7, left).

TT(PhCHO)$_3$ crystallizes in the *C*2/*n* space group with one molecule and a co-crystallized DCM one per asymmetric unit

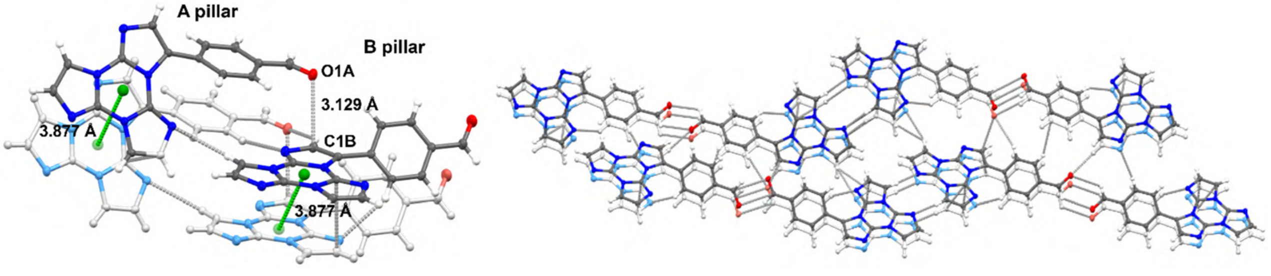

Fig. 7 Fragments of crystal packing of **TTPhCHO** highlighting (left) the stacked motif of A and B molecules, with triazinic centroids plotted as green spheres, and the close carbonyl···TT contact, and (right) two overlapped pairs of HB- and C=O···C=O bonded chains. Intermolecular contacts shorter than the sum of vdW radii are plotted with dashed grey lines. Ellipsoids are drawn at the 20% probability level.

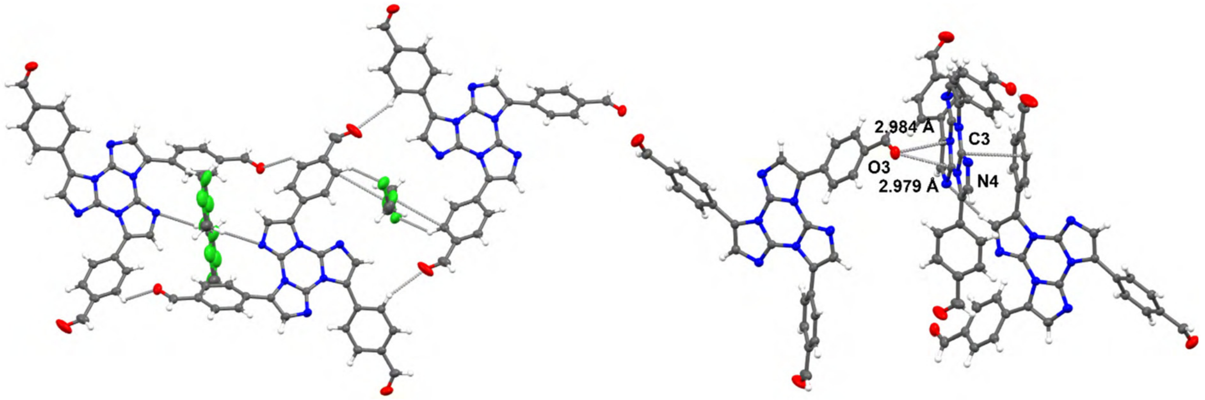

Fig. 8 Fragments of crystal packing of **TT(PhCHO)$_3$** highlighting (left) the HB-bonded units hosting the cocrystilled DCM molecules and (right) the close carbonyl···TT contact and the stacked TT···phenyl motif. Intermolecular contacts shorter than the sum of vdW radii are plotted with dashed grey lines. Ellipsoids are drawn at the 20% probability level (only the main component, A, of the disordered molecule is represented).

(Table S1, Fig. 8 and Fig. S39). Differently from **TTPhCHO**, this structure is highly disordered, essentially due to the possibility of each CHO group to assume both orientations observed in **TTPhCHO**. More precisely, only two of them, *i.e.* those bearing atoms O1 and O2, statistically occupy two positions (A and B) independently of each other (the latter requiring as well to split the bonded phenyl) resulting in four possible conformations (in Fig. 8 only the major components are shown). They display comparable intermolecular interactions with adjacent chromophores (C–H···N and C–H···O HBs) or co-crystallized DCM (C–H···Cl HBs). The third CHO assumes only one position, coinciding with that of A in **TTPhCHO**. The phenyl rings are rotated with respect to the TT plane by 50.0, 43.2 (A) or 39.4 (B), and 50.0°, again showing slightly lower distortion than the isolated conformation as given by DFT calculations (optimized values are 52.0, 50.3 and 53.5°). Molecules of **TT(PhCHO)$_3$** form centrosymmetric dimeric units through relatively short HBs involving two carbonyl groups (those bearing O1A or O1B and O3), which generate relatively large cavities hosting DCM disordered chains (Fig. 8, left). Moreover, molecules stack along *b* by overlapping TT with phenyl units (Fig. 8, right), while neither TT···TT nor CO···CO interactions are present, denoting looser packing with respect to **TTPhCHO**. Finally, a close carbonyl···TT contact is detected also in **TT(PhCHO)$_3$**, with shorter distances with respect to **TTPhCHO** ($r_{O3\cdots N4}$ = 2.979(3) Å, $r_{O3\cdots C3}$ = 2.984(3) Å) but greater angle (37.56°) between carbonyl and TT least-squares planes (see Fig. 8, right).

Therefore, both structures share strong carbonyl···TT interaction which can be recognized at the origin of IEC, resulting in phosphorescence in crystalline samples.[46] It can be proposed that such interactions are responsible for MEP in both **TTPhCHO** and **TT(PhCHO)$_3$**, while LEP can be assigned to π–π (TT-TT and TT-Ph, respectively) interactions. In fact, stacking interactions are associated with low energy phosphorescence in various **TTs** characterized by multiple emissions (a selection of **TTs** with non chromophoric substituents is reported for comparison in Table S4). This interpretation is supported by the strong spectral similarity of **TTPhCHO** LEP with that of **TTs** sharing analogous distances between triazinic centroids (about 3.8 Å), namely **TT** itself,[32] polymorph-H of **TT-2py** (**TT-2pyH**),[52] 3-(2-fluoropyridin-4-yl)triimidazo[1,2-*a*:1′,2′-*c*:1″,2″-*e*][1,3,5]triazine (**TT-4PyF**)[53] and **TT** co-crystallized as guest in **[Zn$_3$(CH$_3$COO)$_6$(H$_2$O)$_2$](TT)$_2$**.[54] All these compounds, in fact, display a vibronically resolved, narrow phosphorescence with peaks covering the 490-620 nm interval (room temperature spectra of crystals of **TTPhCHO**, **TT**, **TT-2pyH** and **[Zn$_3$(CH$_3$COO)$_6$(H$_2$O)$_2$](TT)$_2$** are reported in Fig. 9).

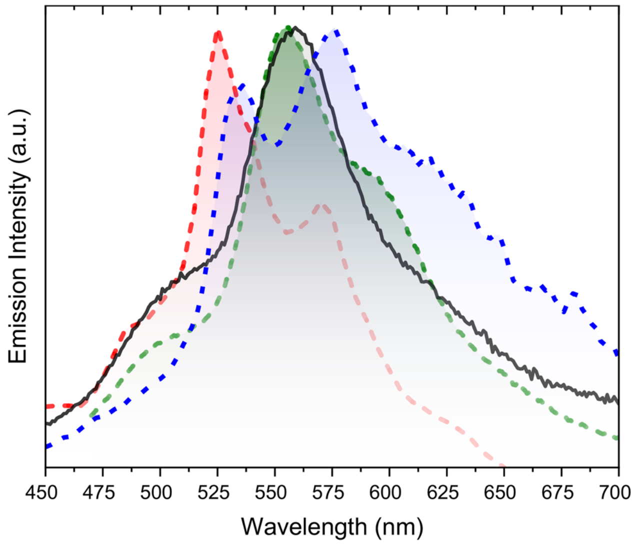

Fig. 9 Normalized emission spectra of crystals at 298 K: **TTPhCHO** (black line: delayed emission, λ_{exc} = 300 nm, delay 50 μs, window 0.5 ms), **[Zn$_3$(CH$_3$COO)$_6$(H$_2$O)$_2$](TT)$_2$** (green dashed line: PL at λ_{exc} = 450 nm), **TT** (red dashed line: delayed emission, λ_{exc} = 374 nm, delay 400 ms, window 1 s) and **TT-2pyH** (blue dashed line: delayed emission, λ_{exc} = 320 nm, delay 1 ms, window 10 ms)

Experimental

All reagents and model molecules were purchased from chemical suppliers and used without further purification unless otherwise stated. **TTBr** and **TTBr$_3$** were prepared according to literature procedures.[55,56]

^1H and ^{13}C NMR spectra were recorded on a Bruker AVANCE-400 instrument (400 MHz). Chemical shifts are reported in parts per million (ppm) and are referenced to the residual solvent peak (CH_2Cl_2, ^1H 5.32 ppm, ^{13}C 54.0 ppm; DMSO, ^1H 2.50 ppm, ^{13}C 39.5 ppm). Coupling constants (J) are given in hertz (Hz) and are quoted to the nearest 0.5 Hz. Peak multiplicities are described in the following way: s, singlet; d, doublet; m, multiplet. Purity of the compounds has been assessed by ^1H-NMR (1024–2048 scans) spectra recorded with ^{13}C decoupling to suppress ^{13}C satellite signals.

Polymethylmethacrylate (PMMA) films were prepared by spin coating (2000 rpm, 60s) a dichloromethane (DCM) solution of the chromophore on a quartz substrate (chromophore/PMMA = 0.5 wt%; PMMA = 10 wt% with respect to the solvent).

Photoluminescence quantum yields have been measured using a C11347 Quantaurus–Absolute Photoluminescence Quantum Yield Spectrometer (Hamamatsu Photonics K.K), equipped with a 150 W Xenon lamp, an integrating sphere and a multichannel detector. Steady state emission and excitation spectra and photoluminescence lifetimes have been obtained using a FLS 980 (Edinburg Instrument Ltd) spectrofluorimeter. The steady state measurements have been recorded by a 450 W Xenon arc lamp. Photoluminescence lifetime measurements have been performed using a EPLED-300 (Edinburg Instrument Ltd) and microsecond flash Xe-lamp (60W, 0.1–100 Hz) with data acquisition devices time correlated single-photon counting (TCSPC) and multichannel scaling (MCS) methods, respectively.

Average lifetimes are obtained $\tau_{\text{av}} = \frac{\sum A_i \tau_i^2}{\sum A_i \tau_i}$ from bi-exponential or three-exponential fits.

Phosphorescence spectra are obtained with a NanoLog composed by a iH320 spectrograph, with PPD-850 single photon detector module and Time-Gated Separation by exciting with a pulsed Xe lamp. The spectra are corrected for the instrument response. Low temperature measurements have been performed by immersion of the sample in a liquid N_2 quartz dewar (steady state measurements) or by using an Oxford DN1704 cryostat (Phosphorescence measurements).

Synthesis of TTPhCHO

TTBr (0.200 g, 0.722 mmol), 4-formylphenylboronic acid MIDA ester (0.207 g, 0.794 mmol), K_2CO_3 (0.997 g, 7.22 mmol), 1,4-dioxane (8 mL) and H_2O (2 mL) were introduced into a 100 mL Schlenk flask equipped with a magnetic stirrer under N_2 atmosphere. To this mixture $Pd(PPh_3)_2Cl_2$ (0.077 g, 0.110 mmol) was further added and the system was heated under static N_2 atmosphere at 100 °C for 4 h. The resulting dark brown reaction mixture was then cooled to room temperature, extracted with dichloromethane, dried with Na_2SO_4 and evaporated to dryness. The crude reaction mixture was purified by chromatography on SiO_2 flash with CH_2Cl_2/CH_3CN as eluents (R_f = 0.30 in CH_2Cl_2/CH_3CN = 8/2) to give **TTPhCHO** as a white solid (0.210 g, 0.695 mmol, Yield: 96%). Single crystals suitable for XRD analysis were obtained by slowly cooling to room temperature a boiling CH_3CN solution of **TTPhCHO**.

NMR data for **TTPhCHO** (9.4 T, CD_2Cl_2, 298 K, δ, ppm): ^1H NMR 10.09 (s, 1H), 7.96 (m, 4H), 7.84 (d, J = 1.6 Hz, 1H), 7.82 (d, J = 1.6 Hz, 1H), 7.33 (s, 1H), 7.30 (d, J = 1.6 Hz, 1H), 7.18 (d, J = 1.6 Hz, 1H). ^{13}C NMR: 192,1 (CHO), 137,3 (C), 136,8 (C), 136,1 (C), 135,9 (C), 134,3 (C), 130,9 (CH), 129,8 (CH), 129,8 (CH), 129,6 (CH), 129,1(CH), 128,5 (C), 112,3 (CH), 111,9 (CH) (Fig. S1-S5).

Synthesis of TT(PhCHO)$_3$

TTBr$_3$ (0.200 g, 0.460 mmol), 4-formylphenylboronic acid MIDA ester (0.372 g, 1.426 mmol), K_2CO_3 (0.636 g, 4.60 mmol), 1,4-dioxane (8 mL) and H_2O (2 mL) were introduced into a 100 mL Schlenk flask equipped with a magnetic stirrer under N_2 atmosphere. To this mixture $Pd(PPh_3)_2Cl_2$ (0.032 g, 0.046 mmol) was further added and the system was heated under static N_2 atmosphere at 100 °C for 4 h. The resulting dark brown reaction mixture was then cooled to room temperature, extracted with dichloromethane, dried with Na_2SO_4 and evaporated to dryness. The crude reaction mixture was purified by chromatography on SiO_2 flash with CH_2Cl_2/CH_3CN as eluents (R_f = 0.34 in CH_2Cl_2/CH_3CN = 9/1) to give **TT(PhCHO)$_3$** as a white solid (0.216 g, 0.423 mmol, Yield: 92%).

Single crystals suitable for XRD analysis were obtained by slowly cooling to room temperature a boiling CH_3CN solution of **TT(PhCHO)$_3$**.

NMR data for **TT(PhCHO)$_3$** (9.4 T, DMSO-d$_6$, 298 K, δ, ppm): ^1H NMR 10.09 (s, 3H), 7.98 (m, 12H), 7.42 (s, 3H). ^{13}C NMR: 192.7 (CHO), 137.5 (C), 135.5 (C), 133.9 (C), 130.0 (CH), 128.9 (CH), 128.8 (CH), 126.6 (C) (Fig. S6–S10).

Single crystal X-ray studies

X-ray data of **TTPhCHO** and **TT(PhCHO)$_3$·CH$_2$Cl$_2$** have been collected on a Rigaku XtaLAB Synergy S X-ray diffractometer (Rigaku Co., Tokyo, Japan) operated with a mirror-monochromated microfocus Cu-Kα radiation (λ = 1.54184 Å) at 50 kV and 1.0 mA and equipped with a CCD HyPix 6000 detector. The structure has been solved using direct methods and refined with SHELXL-19[57] using a full-matrix least squares procedure based on F^2 using all data. Hydrogen atoms have been placed at geometrically estimated positions. Details relating to the crystal and the structural refinement are presented in Table S1. Full details of crystal data and structure refinement, in CIF format, are available as Supplementary Information. CCDC reference numbers: 2500777 (**TTPhCHO**) and 2500778 (**TT(PhCHO)$_3$·CH$_2$Cl$_2$**).

Computational studies

DFT and TDDFT calculations on **TTPhCHO** and **TT(PhCHO)$_3$** were performed with Gaussian 16 program (Revision C.01)[58] using the 6-311++G(d,p) basis set, starting from the corresponding X-ray molecular structures. Based on previous theoretical results as obtained on the parent cyclic triimidazole and its derivatives,[47] DFT calculations have been carried out with the ωB97X functional,[59] which was demonstrated to be suitable to correctly treat, at the same time, not only ground and excited states properties (though quite overestimating the excitation energies), but also intermolecular interactions, in particular H-bonding and π–π stacking interactions, which play a key role in the photophysics of **TT** and its derivatives. The spin–orbit coupling (SOC) matrix elements between singlet and triplet excited states were computed on the S_1 and S_1' optimized geometries using ORCA 5.0.3.[60]

Conclusions

The PhCHO mono- and tri-substituted derivatives of cyclic triimidazole here reported represent intriguing examples of purely organic RTP systems being characterized in their crystalline state by only long-lived features which, in **TTPhCHO**, result in bright phosphorescence (Φ = 7%). Molecular and supramolecular emissions are disclosed for both compounds through computational studies and structural analysis. A high energy phosphorescence of molecular origin is present for both compounds in solid phases, while packing features result in MEP and LEP supramolecular contributions. CO–π interactions, present in the crystal structure of both compounds, activate IEC mechanisms resulting in MEP. On the other side, TT-TT (in **TTPhCHO**) and TT-Ph (in **TT(PhCHO)$_3$**) π–π stacking interactions are at the basis of LEP. These results represent a step forward in the rationalization of RTP emissions from purely organic materials and therefore in the development of new materials to be used in electronic and photonic innovative fields.

Author contributions

Conceptualization, D. Mal., E. C. and A. F.; methodology, D. Mal., E. L., E. C. and A. F.; investigation, all authors; supervision, E. C. and A. F.; writing – original draft preparation: E. C. and A. F.; writing – review and editing: all authors.

Conflicts of interest

There are no conflicts to declare.

Data availability

The data supporting this article have been included as part of the supplementary information (SI). Supplementary information: NMR spectra, photophysical data, computational results and crystallographic data. See DOI: **https://doi.org/10.1039/d5qm00794a**.

CCDC 2500777 and 2500778 contain the supplementary crystallographic data for this paper.[61a,b]

Acknowledgements

D. Mal. acknowledges Fondazione Cariplo for financial support (Giovani Ricercatori, 2024-0439). The use of instrumentation purchased through the Regione Lombardia – Fondazione Cariplo joint SmartMatLab Project is gratefully acknowledged. XRD data have been collected at the SCXRD facility of the Unitech COSPECT at the University of Milan (Italy). This work was supported by the University of Milan (Project PSR2023_DIP_005_PI_FTESS).

Notes and references

1 N. Gan, X. Zou, Z. Qian, A. Lv, L. Wang, H. Ma, H.-J. Qian, L. Gu, Z. An and W. Huang, Stretchable phosphorescent polymers by multiphase engineering, *Nat. Commun.*, 2024, **15**, 4113.

2 J. Sun, H. Ahn, S. Kang, S.-B. Ko, D. Song, H. A. Um, S. Kim, Y. Lee, P. Jeon, S.-H. Hwang, Y. You, C. Chu and S. Kim, Exceptionally stable blue phosphorescent organic light-emitting diodes, *Nat. Photon.*, 2022, **16**, 212–218.

3 W. Zhao, Z. He and B. Z. Tang, Room-temperature phosphorescence from organic aggregates, *Nat. Rev. Mater.*, 2020, **5**, 869–885.

4 X.-Y. Dai, M. Huo and Y. Liu, Phosphorescence resonance energy transfer from purely organic supramolecular assembly, *Nat. Rev. Chem.*, 2023, **7**, 854–874.

5 J. Guo, C. Yang and Y. Zhao, Long-Lived Organic Room-Temperature Phosphorescence from Amorphous Polymer Systems, *Acc. Chem. Res.*, 2022, **55**, 1160–1170.

6 J. Huang, L. Qu, L. Gao, X. Wang, Q. Chen, Y. Wang, Y. Zhu, C. Li, Y. Li and C. Yang, Multicolor Room-Temperature Phosphorescence Achieved by Intrinsic Polymers Containing Solely One Phosphor Unit, *Macromolecules*, 2024, **57**, 5018–5027.

7 X. Luo, B. Tian, Y. Zhai, H. Guo, S. Liu, J. Li, S. Li, T. D. James and Z. Chen, Room-temperature phosphorescent materials derived from natural resources, *Nat. Rev. Chem.*, 2023, **7**, 800–812.

8 Z. Ruan, Q. Liao, Q. Dang, X. Chen, C. Deng, Z. Gao, J. Lin, S. Liu, Y. Chen, Z. Tian and Z. Li, Luminous Butterflies: Rational Molecular Design to Optimize Crystal Packing for Dramatically Enhanced Room-Temperature Phosphorescence, *Adv. Opt. Mater.*, 2021, **9**, 2001549.

9 Z.-P. Song, J. Wei, J. Liu, Z.-F. Chu, J.-X. Hu, S. Chakraborty, Y. Ma, B.-X. Li, Y.-Q. Lu and Q. Zhao, Mechanically-Tunable and Full-Color Circularly Polarized Long-Lived Phosphorescence in Chiral Superstructure Elastomers, *Adv. Mater.*, 2025, **37**, 2419640.

10 J. Yang, M. Fang and Z. Li, Stimulus-Responsive Room Temperature Phosphorescence Materials: Internal Mechanism, Design Strategy, and Potential Application, *Acc. Mater. Res.*, 2021, **2**, 644–654.

11 B. Chang, J. Chen, J. Bao, T. Sun and Z. Cheng, Molecularly Engineered Room-Temperature Phosphorescence for Biomedical Application: From the Visible toward Second Near-Infrared Window, *Chem. Rev.*, 2023, **123**, 13966–14037.

12 X. Dou, X. Wang, X. Xie, J. Zhang, Y. Li and B. Tang, Advances in Polymer-Based Organic Room-Temperature Phosphorescence Materials, *Adv. Funct. Mater.*, 2024, **34**, 2314069.

13 Z. He, H. Gao, S. Zhang, S. Zheng, Y. Wang, Z. Zhao, D. Ding, B. Yang, Y. Zhang and W. Z. Yuan, Achieving Persistent, Efficient, and Robust Room-Temperature Phosphorescence

from Pure Organics for Versatile Applications, *Adv. Mater.*, 2019, **31**, 1807222.

14 Y. Hou, G. Jiang, J. Gong, R. Sha and J. Wang, Recent Advances of Pure Organic Room Temperature Phosphorescence Materials for Bioimaging Applications, *Chem. Res. Chin. Univ.*, 2021, **37**, 73–82.

15 X.-Q. Liu, K. Zhang, J.-F. Gao, Y.-Z. Chen, C.-H. Tung and L.-Z. Wu, Monochromophore-Based Phosphorescence and Fluorescence from Pure Organic Assemblies for Ratiometric Hypoxia Detection, *Angew. Chem., Int. Ed.*, 2020, **59**, 23456–23460.

16 J. Yang, H. Gao, Y. Wang, Y. Yu, Y. Gong, M. Fang, D. Ding, W. Hu, B. Z. Tang and Z. Li, The odd–even effect of alkyl chain in organic room temperature phosphorescence luminogens and the corresponding in vivo imaging, *Mater. Chem. Front.*, 2019, **3**, 1391–1397.

17 Z. Guan, Z. Tang, Z. Yao, Q. Guo, S. Zhang, Z. Lv, X. Zhang, N. Ma, X. Liu and Z. Hu, ''Rigid-Flexible'' Strategy Realizes Robust Ultralong Phosphorescence for Multifunctional Display Unit and Photoreceptor Synapse, *Adv. Mater.*, 2025, **37**, e07192.

18 Q. Qi, J. T. Plank, A. R. Lippert and I. Aprahamian, A photoswitchable handheld volumetric 3D display, *Chem*, 2024, **10**, 3575–3581.

19 H. Sun, Y. Xiao, Y. He, X. Wei, J. Zou, Y. Luo, Y. Wu, J. Zhao, V. K.-M. Au and T. Yu, 3D printable organic room-temperature phosphorescent materials and printed real-time sensing and display devices, *Chem. Sci.*, 2025, **16**, 5299–5309.

20 S. Wan, H. Zhou, J. Lin and W. Lu, A Prototype of a Volumetric Three-Dimensional Display Based on Programmable Photo-Activated Phosphorescence, *Angew. Chem., Int. Ed.*, 2020, **59**, 8416–8420.

21 M. Ji and X. Ma, Recent progress with the application of organic room-temperature phosphorescent materials, *Ind. Chem. Mater.*, 2023, **1**, 582–594.

22 Y. Yang, Q. Li and Z. Li, Advances in organic room-temperature phosphorescence: design strategies, photophysical mechanisms, and emerging applications, *Mater. Chem. Front.*, 2025, **9**, 744–753.

23 C. Ren, Z. Wang, T. Wang, J. Guo, Y. Dai, H. Yuan and Y. Tan, Ultralong Organic Phosphorescence Modulation of Aromatic Carbonyls and Multi-Component Systems, *Chin. J. Chem.*, 2022, **40**, 1987–2000.

24 Y. Gong, G. Chen, Q. Peng, W. Z. Yuan, Y. Xie, S. Li, Y. Zhang and B. Z. Tang, Achieving Persistent Room Temperature Phosphorescence and Remarkable Mechanochromism from Pure Organic Luminogens, *Adv. Mater.*, 2015, **27**, 6195–6201.

25 W. Z. Yuan, X. Y. Shen, H. Zhao, J. W. Y. Lam, L. Tang, P. Lu, C. Wang, Y. Liu, Z. Wang, Q. Zheng, J. Z. Sun, Y. Ma and B. Z. Tang, Crystallization-Induced Phosphorescence of Pure Organic Luminogens at Room Temperature, *J. Phys. Chem. C*, 2010, **114**, 6090–6099.

26 X. Bi, Y. Xiong and B. Z. Tang, Recent advances in room-temperature phosphorescence metal–organic frameworks: structural design, property modulation, and emerging applications, *Mater. Chem. Front.*, 2026, DOI: **10.1039/D5QM00773A**.

27 S. Hirata, K. Totani, J. Zhang, T. Yamashita, H. Kaji, S. R. Marder, T. Watanabe and C. Adachi, Efficient Persistent Room Temperature Phosphorescence in Organic Amorphous Materials under Ambient Conditions, *Adv. Funct. Mater.*, 2013, **23**, 3386–3397.

28 Y. Su, S. Z. F. Phua, Y. Li, X. Zhou, D. Jana, G. Liu, W. Q. Lim, W. K. Ong, C. Yang and Y. Zhao, Ultralong room temperature phosphorescence from amorphous organic materials toward confidential information encryption and decryption, *Sci. Adv.*, 2018, **4**, eaas9732.

29 H. Thomas, D. L. Pastoetter, M. Gmelch, T. Achenbach, A. Schlögl, M. Louis, X. Feng and S. Reineke, Aromatic Phosphonates: A Novel Group of Emitters Showing Blue Ultralong Room Temperature Phosphorescence, *Adv. Mater.*, 2020, **32**, 2000880.

30 X. Zhang, L. Du, W. Zhao, Z. Zhao, Y. Xiong, X. He, P. F. Gao, P. Alam, C. Wang, Z. Li, J. Leng, J. Liu, C. Zhou, J. W. Y. Lam, D. L. Phillips, G. Zhang and B. Z. Tang, Ultralong UV/mechano-excited room temperature phosphorescence from purely organic cluster excitons, *Nat. Commun.*, 2019, **10**, 5161.

31 Z. An, C. Zheng, Y. Tao, R. Chen, H. Shi, T. Chen, Z. Wang, H. Li, R. Deng, X. Liu and W. Huang, Stabilizing triplet excited states for ultralong organic phosphorescence, *Nat. Mater.*, 2015, **14**, 685–690.

32 E. Lucenti, A. Forni, C. Botta, L. Carlucci, C. Giannini, D. Marinotto, A. Previtali, S. Righetto and E. Cariati, H-Aggregates Granting Crystallization-Induced Emissive Behavior and Ultralong Phosphorescence from a Pure Organic Molecule, *J. Phys. Chem. Lett.*, 2017, **8**, 1894–1898.

33 X. Ma, C. Xu, J. Wang and H. Tian, Amorphous Pure Organic Polymers for Heavy-Atom-Free Efficient Room-Temperature Phosphorescence Emission, *Angew. Chem., Int. Ed.*, 2018, **57**, 10854–10858.

34 J. Liu, Z.-P. Song, J. Wei, J.-J. Wu, M.-Z. Wang, J.-G. Li, Y. Ma, B.-X. Li, Y.-Q. Lu and Q. Zhao, Circularly Polarized Organic Ultralong Room-Temperature Phosphorescence with A High Dissymmetry Factor in Chiral Helical Superstructures, *Adv. Mater.*, 2024, **36**, 2306834.

35 D.-X. Ma, Z.-Q. Li, K. Tang, Z.-L. Gong, J.-Y. Shao and Y.-W. Zhong, Nylons with Highly-Bright and Ultralong Organic Room-Temperature Phosphorescence, *Nat. Commun.*, 2024, **15**, 4402.

36 G. Yang, S. Hao, X. Deng, X. Song, B. Sun, W. J. Hyun, M.-D. Li and L. Dang, Efficient intersystem crossing and tunable ultralong organic room-temperature phosphorescence via doping polyvinylpyrrolidone with polyaromatic hydrocarbons, *Nat. Commun.*, 2024, **15**, 4674.

37 T. Zhang, Y. Jing, Z. Wang, W. Wu, Y. L. Pak, X. Gao, Y. Guo and J. Song, Room-temperature phosphorescence based on doping systems: material design, mechanisms, and applications, *Mater. Chem. Front.*, 2026, DOI: **10.1039/D5QM00552C**.

38 Z. Wang, Y. Wang, W. Mo, L. Jin and W. Hong, Mechano-responsive 3D-printed organic afterglow systems with programmable color output, *Chem. Eng. J.*, 2025, **522**, 168120.

39 X. Yao, H. Ma, X. Wang, H. Wang, Q. Wang, X. Zou, Z. Song, W. Jia, Y. Li, Y. Mao, M. Singh, W. Ye, J. Liang, Y. Zhang, Z. Liu, Y. He, J. Li, Z. Zhou, Z. Zhao, Y. Zhang, G. Niu, C. Yin,

S. Zhang, H. Shi, W. Huang and Z. An, Ultralong organic phosphorescence from isolated molecules with repulsive interactions for multifunctional applications, *Nat. Commun.*, 2022, **13**, 4890.

40 S. Zhang, Y. Ji, S. Chen, S. Chen, D. Xiao, C. Chen, G. Guo, M. Zeng, W. Wang, J. Zhang, H. Li, Y. Tao, G. Xie, H. Li, Y. Zhang, R. Chen and W. Huang, Universal in situ supersaturated crystallization enables 3D printable afterglow hydrogel, *npj Flex Electron*, 2025, **9**, 8.

41 W. Li, Q. Huang, Z. Mao, X. He, D. Ma, J. Zhao, J. W. Y. Lam, Y. Zhang, B. Z. Tang and Z. Chi, A dish-like molecular architecture for dynamic ultralong room-temperature phosphorescence through reversible guest accommodation, *Nat. Commun.*, 2022, **13**, 7423.

42 D. Malpicci, A. Forni, C. Botta, C. Giannini, E. Lucenti, D. Marinotto, D. Maver, L. Carlucci and E. Cariati, Dual fluorescence and RTP features of carbazole-cyclic triimidazole derivatives: The fluorophores' connectivity does matter, *Dyes Pigm.*, 2023, **215**, 111274.

43 D. Malpicci, D. Maver, E. Rosadoni, A. Colombo, E. Lucenti, D. Marinotto, C. Botta, F. Bellina, E. Cariati and A. Forni, 3-Ethynyltriimidazo[1,2-*a*:1′,2′-*c*:1″,2″-*e*][1,3,5]triazine Dual Short- and Long-Lived Emissions with Crystallization-Enhanced Feature: Role of Hydrogen Bonds and π–π Interactions, *Molecules*, 2024, **29**, 1967.

44 K. Ramamurthy, E. J. P. Malar and C. Selvaraju, Hydrogen bonded dimers of ketocoumarin in the solid state and alcohol:-water binary solvent: fluorescence spectroscopy, crystal structure and DFT investigation, *New J. Chem.*, 2019, **43**, 9090–9105.

45 W. Wang, Y. Zhang and W. J. Jin, Halogen bonding in room-temperature phosphorescent materials, *Coord. Chem. Rev.*, 2020, **404**, 213107.

46 Z. Yang, Z. Mao, X. Zhang, D. Ou, Y. Mu, Y. Zhang, C. Zhao, S. Liu, Z. Chi, J. Xu, Y.-C. Wu, P.-Y. Lu, A. Lien and M. R. Bryce, Intermolecular Electronic Coupling of Organic Units for Efficient Persistent Room-Temperature Phosphorescence, *Angew. Chem., Int. Ed.*, 2016, **55**, 2181–2185.

47 A. Forni, D. Malpicci, D. Maver, E. Lucenti and E. Cariati, The intriguing case of cyclic triimidazole: an emerging scaffold for the preparation of multiemissive, bio-medical and hybrid inorganic–organic materials, *J. Mater. Chem. C*, 2025, **13**, 3721–3758.

48 D. Malpicci, S. Di Ciolo, E. Cariati, E. Lucenti, D. Marinotto, D. Maver, C. Giannini, L. Carlucci, C. Botta and A. Forni, Role of molecular packing in RTP features of positional isomers: The case study of triimidazo-triazine functionalized with ethynyl pyridine moieties, *Next Mater.*, 2025, **7**, 100440.

49 E. Lucenti, A. Forni, C. Botta, C. Giannini, D. Malpicci, D. Marinotto, A. Previtali, S. Righetto and E. Cariati, Intrinsic and Extrinsic Heavy-Atom Effects on the Multifaceted Emissive Behavior of Cyclic Triimidazole, *Chem. – Eur. J.*, 2019, **25**, 2452–2456.

50 J. Jovaišaitė, S. Kirschner, S. Raišys, G. Kreiza, P. Baronas, S. Juršėnas and M. Wagner, Diboraanthracene-Doped Polymer Systems for Colour-Tuneable Room-Temperature Organic Afterglow, *Angew. Chem., Int. Ed.*, 2023, **62**, e202215071.

51 M. O'Keeffe, Sphere Packings and Space Filling by Congruent Simple Polyhedra, *Acta Crystallogr., Sect. A:Found. Crystallogr.*, 1998, **54**, 320–329.

52 E. Lucenti, A. Forni, A. Previtali, D. Marinotto, D. Malpicci, S. Righetto, C. Giannini, T. Virgili, P. Kabacinski, L. Ganzer, U. Giovanella, C. Botta and E. Cariati, Unravelling the intricate photophysical behavior of 3-(pyridin-2-yl)triimidazotriazine AIE and RTP polymorphs, *Chem. Sci.*, 2020, **11**, 7599–7608.

53 A. Previtali, E. Lucenti, A. Forni, L. Mauri, C. Botta, C. Giannini, D. Malpicci, D. Marinotto, S. Righetto and E. Cariati, Solid State Room Temperature Dual Phosphorescence from 3-(2-Fluoropyridin-4-yl)triimidazo[1,2-*a*:1′,2′-*c*:1″,2″-*e*][1,3,5]triazine, *Molecules*, 2019, **24**, 2552.

54 E. Cariati, A. Forni, E. Lucenti, D. Marinotto, A. Previtali, S. Righetto, C. Botta, V. Bold, V. Kravtsov and M. S. Fonari, Extrinsic Heavy Metal Atom Effect on the Solid-State Room Temperature Phosphorescence of Cyclic Triimidazole, *Chem. – Asian J.*, 2019, **14**, 853–858.

55 E. Lucenti, A. Forni, C. Botta, L. Carlucci, A. Colombo, C. Giannini, D. Marinotto, A. Previtali, S. Righetto and E. Cariati, The effect of bromo substituents on the multifaceted emissive and crystal-packing features of cyclic triimidazole derivatives, *ChemPhotoChem*, 2018, **2**, 801–805.

56 E. Lucenti, A. Forni, C. Botta, L. Carlucci, C. Giannini, D. Marinotto, A. Pavanello, A. Previtali, S. Righetto and E. Cariati, Cyclic Triimidazole Derivatives: Intriguing Examples of Multiple Emissions and Ultralong Phosphorescence at Room Temperature, *Angew. Chem., Int. Ed.*, 2017, **56**, 16302–16307.

57 G. M. Sheldrick, Crystal structure refinement with SHELXL, *Acta Crystallogr., Sect. C:Struct. Chem.*, 2015, **71**, 3–8.

58 M. J. Frisch, G. W. Trucks, H. B. Schlegel, G. E. Scuseria, M. A. Robb, J. R. Cheeseman, G. Scalmani, V. Barone, G. A. Petersson, H. Nakatsuji, X. Li, M. Caricato, A. V. Marenich, J. Bloino, B. G. Janesko, R. Gomperts, B. Mennucci, H. P. Hratchian, J. V. Ortiz, A. F. Izmaylov, J. L. Sonnenberg Williams, F. Ding, F. Lipparini, F. Egidi, J. Goings, B. Peng, A. Petrone, T. Henderson, D. Ranasinghe, V. G. Zakrzewski, J. Gao, N. Rega, G. Zheng, W. Liang, M. Hada, M. Ehara, K. Toyota, R. Fukuda, J. Hasegawa, M. Ishida, T. Nakajima, Y. Honda, O. Kitao, H. Nakai, T. Vreven, K. Throssell, J. A. Montgomery Jr., J. E. Peralta, F. Ogliaro, M. J. Bearpark, J. J. Heyd, E. N. Brothers, K. N. Kudin, V. N. Staroverov, T. A. Keith, R. Kobayashi, J. Normand, K. Raghavachari, A. P. Rendell, J. C. Burant, S. S. Iyengar, J. Tomasi, M. Cossi, J. M. Millam, M. Klene, C. Adamo, R. Cammi, J. W. Ochterski, R. L. Martin, K. Morokuma, O. Farkas, J. B. Foresman and D. J. Fox, *Gaussian 16 Rev. C.01*, Gaussian Inc., Wallingford, CT, USA, 2019.

59 J.-D. Chai and M. Head-Gordon, Systematic optimization of long-range corrected hybrid density functionals, *J. Chem. Phys.*, 2008, **128**, 84106.

60 F. Neese, The ORCA program system, *WIREs Comput. Mol. Sci.*, 2012, **2**, 73–78.

61 (*a*) CCDC 2500777: Experimental Crystal Structure Determination, 2026, DOI: **10.5517/ccdc.csd.cc2py875**; (*b*) CCDC 2500778: Experimental Crystal Structure Determination, 2026, DOI: **10.5517/ccdc.csd.cc2py886**.